Nanoscale

PAPER

View Article Online
View Journal | View Issue

Cite this: *Nanoscale*, 2015, **7**, 15385

Tuning the electronic properties of transition-metal trichalcogenides *via* tensile strain†

Ming Li,[a,b] Jun Dai[b] and Xiao Cheng Zeng*[b]

Received 6th July 2015,
Accepted 12th August 2015

DOI: 10.1039/c5nr04505c

www.rsc.org/nanoscale

A comprehensive study of the effect of tensile strain (ε = 0% to 8%) on the electronic structures of two-dimensional (2D) transition-metal trichalcogenide (TMTC) monolayers MX_3 (M = Ti, Zr, Hf, Nb; X = S, Se Te) is performed on the basis of density functional theory (DFT) computation. The unstrained TiS_3, ZrS_3, $ZrSe_3$, HfS_3, $HfSe_3$ and NbS_3 monolayers are predicted to be semiconductors with their bandgap ranging from 0.80 to 1.94 eV. Our DFT computations show that the biaxial and uniaxial tensile strains can effectively modify the bandgap of many TMTC monolayers. In particular, we find that ZrS_3 and HfS_3 monolayers undergo an indirect-to-direct bandgap transition with increasing tensile strain. The indirect bandgaps of $ZrSe_3$ and $HfSe_3$ monolayers also increase with the tensile strain. Both $ZrTe_3$ and $HfTe_3$ monolayers are predicted to be metals, but can be transformed into indirect bandgap semiconductors at ε = 4% and ε = 6%, respectively. Importantly, the TiS_3 monolayer can retain its direct-bandgap feature over a range of biaxial or uniaxial tensile strains (up to 8%). The highly tunable direct bandgaps of MS_3 (M = Hf, Ti, and Zr) by strain and the availability of metallic and semiconducting properties of MTe_3 (M = Hf and Zr) provide exciting opportunities for designing artificial layered structures for applications in optoelectronics and flexible electronics.

Introduction

In recent years, 2D layered nanomaterials have attracted intensive interest due to their novel electronic, optical, thermal, and mechanical properties for potential applications in various fields. With regard to transition-metal based 2D materials, thus far, predominant investigations have been focused on the transition metal dichalcogenides (TMDCs) such as MoS_2, not only because of their novel electronic and catalytic properties but also their high tunability *via* strain or a vertical electric field.[1–6] Remarkably, large-scale growth of monolayered MoS_2 films with spatial homogeneity and high electrical performance has been recently demonstrated in the laboratory.[7] It has also been demonstrated that MoS_2 exhibits many exotic characteristics that are absent in its bulk counterpart.[8–10] MoS_2 is a semiconductor with a direct bandgap, although the bulk MoS_2 possesses an indirect bandgap.[11] The direct bandgap character of 2D layered materials such as monolayered MoS_2 is highly desired for applications in thinner transistors, thermoelectrics and solar cells. Towards this end, several new chemical approaches to contrive new 2D nanomaterials have been reported,[12–14] which renders synthesis of new monolayered nanomaterials more accessible.

Like TMDCs, many bulk transition metal trichalcogenides (TMTCs) exhibit layered structures with weak interlayer van der Waals interactions. Most TMTCs, *i.e.* MX_3 (M = Ti, Zr, Hf; X = S, Se, Te), possess monoclinic crystalline structures with the space group $P2_1/m$,[15,16] while the space group of NbS_3 is $P1$ and its most stable crystalline structure is triclinic.[17,18] Although many bulk MX_3 compounds have been studied for several decades,[19–26] 2D MX_3 layered materials have received little attention until very recently when the new monolayered TiS_3 was isolated,[27,28] and was also predicted to possess exciting electronic properties such as a direct band gap (1.06 eV) close to that of silicon.[29] Note that the bulk TiS_3 is an n-type semiconductor with an indirect band gap. Previous studies also showed that TiS_3 possesses lower cleavage energy than graphite.[29,30] Indeed, Island *et al.* demonstrated that a TiS_3 film can be exfoliated down to single layers with high photoresponse and fast switching rates.[31]

As pointed out previously, 2D layered semiconducting materials with direct and tunable bandgaps are highly desired for nanoelectronic and optoelectronic applications.[32–38] It is known that engineering 2D layered materials by strain is a viable approach to achieve tunable electronic properties.[39–46] Over the past few years, effects of strains on electronic

[a]*College of Chemical engineering, North China University of Science and Technology, Tang shan, Hebei 063000, China*
[b]*Department of Chemistry and Department Mechanics and Materials Engineering, University of Nebraska-Lincoln, Lincoln, NE 68588, USA. E-mail: xzeng1@unl.edu*
†Electronic supplementary information (ESI) available. See DOI: 10.1039/c5nr04505c

properties of TMDCs have been extensively studied, especially from the theoretical viewpoint.[47–53] It was predicted that some TMDC monolayers can undergo an indirect-to-direct bandgap transition under the tensile strain. Hence, it is timely and important to explore whether the indirect-to-direct bandgap transition can occur when TMTC monolayers are under tensile strain. In this study, effects of both biaxial and uniaxial strains on the bandgap of a series of MX_3 monolayers (M = Ti, Zr, Hf, Nb; X = S, Se, Te) are investigated. We find that as in the case of TMDCs, the tensile strains can strongly modify the bandgap of many TMTC monolayers.

Computational methods

All computations were performed within the framework of density functional theory (DFT), using the Vienna ab initio simulation package (VASP 5.3).[54] The core–valence interaction was described by the projector augmented wave (PAW) method.[55] The generalized gradient approximation (GGA) in the form of Becke86 was adopted for the exchange–correlation functional.[56] More specifically, the optB86b-vdW functional, implemented to account for weak van der Waals (vdW) interactions,[57] was used for structure optimization (we also examined two other GGA functionals with the vdW correction, namely optPBE-vdW and optB88-vdW, and found that the optB86b-vdW functional gives the best agreement with experiments in predicting the lattice constants of bulk TMTCs). It is known that GGA functionals tend to underestimate the band gap of semiconductors. So the electronic structures were computed using the Heyd–Scuseria–Ernzerhof (HSE06) hybrid functional.[58] The same computations were also performed with the optB86-vdW functional to confirm the general trend of strain-dependent bandgaps. Energy cut off for the plane-wave expansion was set to 500 eV. Brillouin zone sampling was performed with Monkhorst–Pack (MP) special k-point meshes. The 2D Brillouin zone integration using the Γ-center scheme was sampled with a 7 × 10 × 1 grid for geometry optimizations (7 × 10 × 4 for bulk systems), and the k-point grid scaled with respect to the supercell size. A vacuum layer greater than 15 Å was taken to avoid interaction between adjacent images. All atoms were allowed to relax during the geometry optimization until the computed Hellmann–Feynman force on each atom was smaller than 0.02 eV $Å^{-1}$. The convergence threshold was set as 10^{-4} eV in energy. Spin–orbit coupling (SOC) was included when computing the band structures. Tensile strain ranging from 0 to 8% was considered. The tensile strain was undertaken in three different ways: (1) biaxial expansion in both the x and y directions (xy), uniaxial expansion of the monolayer in the x direction (xx) or the y direction (yy).[51] For the uniaxial strain, the Poisson effect is considered. The strain scale is defined as $\varepsilon = \Delta m/m_0$. For biaxial tensile strain, m_0 is the unstrained cell parameter, and $\Delta m + m_0$ is the strained cell parameter. For uniaxial tensile strain, m_0 is the projection of the unit-cell vector in the x or y direction, and Δm is the associated change from m_0.

Results and discussion

As mentioned above, the optimized lattice vectors based on the optB86b-vdW functional agree well with the experimental data. For example, the optimized lattice constants of ZrS_3 bulk are a_0 = 5.133 Å, b_0 = 3.624 Å, c_0 = 9.008 Å, and β = 97.15°, in good agreement with the experimental values (a_0 = 5.124 Å, b_0 = 3.624 Å, c_0 = 8.980 Å, and β = 97.28°). Note that the TMTC bulks often have many allotropes.[15–17] In this study, we only consider TMTC monolayers cleaved from the most stable bulk allotrope at 0 K. For TiX_3, ZrX_3, and HfX_3, the most stable crystalline structure is monoclinic, while for NbS_3 the most stable crystalline structure is triclinic. Next, the band structures of MX_3 bulks are computed using the HSE06 functional. The HSE06 bandgaps of TiS_3, ZrS_3, $ZrSe_3$, HfS_3, $HfSe_3$ and NbS_3 bulks are 1.05 eV, 1.87 eV, 0.68 eV, 1.90 eV, 0.59 eV and 1.07 eV, respectively, in good agreement with the measured bandgaps from experiments.[32–38] For example, the measured bandgap of ZrS_3 and HfS_3 is 1.91 and 1.95 eV, respectively.

The optimized lattice constants of TMTC monolayers (see Fig. 1 for structures) based on the optB86b-vdW functional are summarized in Table 1, together with the computed HSE06 bandgaps. For the band-structure computation, the Brillouin zone of ΓYAΓB (Fig. 1c) is selected.

As shown in Table 1, the unstained TiS_3 monolayer is the only TMTC considered with a direct bandgap. Table 1 also shows that ZrS_3, $ZrSe_3$, HfS_3, $HfSe_3$, and NbS_3 monolayers are also semiconductors but with an indirect bandgap. $ZrTe_3$ and $HfTe_3$ are predicted to have the electronic structures of metals. Previously, we have examined the dynamical stability of the TiS_3 monolayer by computing its phonon spectrum.[29] Here we have also computed the phonon spectrum of two prototype monolayers, HfS_3 and $HfSe_3$, one is the direct semiconductor under biaxial strain while another is the indirect semiconductor under all types of strain. As shown in ESI Fig. S1,† there is no negative frequency in the computed phonon spectrum of HfS_3 and $HfSe_3$ monolayers.

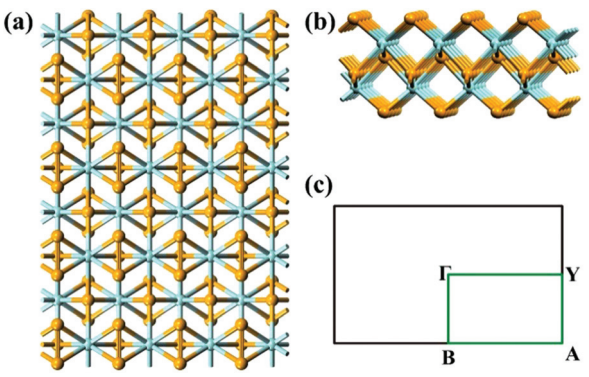

Fig. 1 (a) Top view and (b) side view of a 4 × 4 MX_3 monolayered sheet, (c) the first Brillouin zone and the high symmetry points associated with the MX_3 monolayer. The ocher and cyan spheres refer to M and X atoms, respectively.

Table 1 Optimized lattice constants a_0 (Å) and b_0 (Å) of MX_3 monolayers (M = Ti, Zr, Hf, Nb; X = S, Se, Te), based on the optB86b-vdW functional, and computed bandgaps, based on the HSE06 functional. The direct or indirect bandgap is also denoted by D or I

	a_0 (Å)	b_0 (Å)	Bandgap (eV)	Direct/indirect
ZrS_3	5.138	3.619	1.92	I
$ZrSe_3$	5.423	3.745	0.92	I
$ZrTe_3$	5.942	3.909	Metal	—
HfS_3	5.092	3.576	1.94	I
$HfSe_3$	5.402	3.709	0.80	I
$HfTe_3$	5.941	3.882	Metal	—
TiS_3	4.970	3.386	1.08	D
NbS_3	4.992	6.746	1.18	I

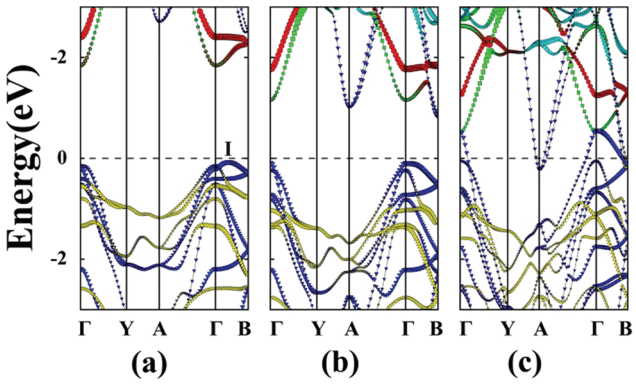

Fig. 3 Band structures of unstrained monolayers (a) ZrS_3, (b) $ZrSe_3$, and (c) $ZrTe_3$. The red lines denote the d_{z^2} orbital of the Zr atom. The green lines denote the $d_{x^2-y^2}$ orbitals of the Zr atom. The cyan lines denote the d_{xy}, d_{yz} and d_{xz} orbitals of the Zr atom. The blue lines denote the p_x and p_y orbitals of (a) S, (b) Se, (c) and Te atoms, and the yellow lines denote the p_z orbital of (a) S, (b) Se, and (c) Te atoms. The dashed lines indicate the Fermi level. The I point refers to the VBM not located at the Γ point.

Next, the effect of tensile strain on the electronic structures of MX_3 monolayers (M = Zr, Hf; X = S, Se Te) is investigated in detail. The computed HSE06 bandgaps of MX_3 monolayers (M = Zr, Hf; X = S, Se Te), subjected to biaxial or uniaxial strain ranging from 0% to 8% are summarized in Fig. 2.

ZrX_3 and HfX_3

The unstrained ZrS_3 monolayer is a semiconductor with an indirect bandgap of 1.92 eV. As shown in Fig. 3(a), the conduction band minimum (CBM) and valence band maximum (VBM) are located at Γ point and I point, respectively. Here, the energy at I point is only 0.07 eV higher than that at the Γ point. The CBM is mainly contributed by d_{z^2} and $d_{x^2-y^2}$ orbitals of the Zr atom, while the VBM is mainly contributed by p_x and p_y orbitals of the S atom. The partial density of states (PDOS) is depicted in ESI Fig. S2.†

When the ZrS_3 monolayer is subjected to the biaxial tensile strain of ε = 2% in both the x and y directions, its bandgap increases to 2.08 eV. More interestingly, as illustrated in Fig. 4,

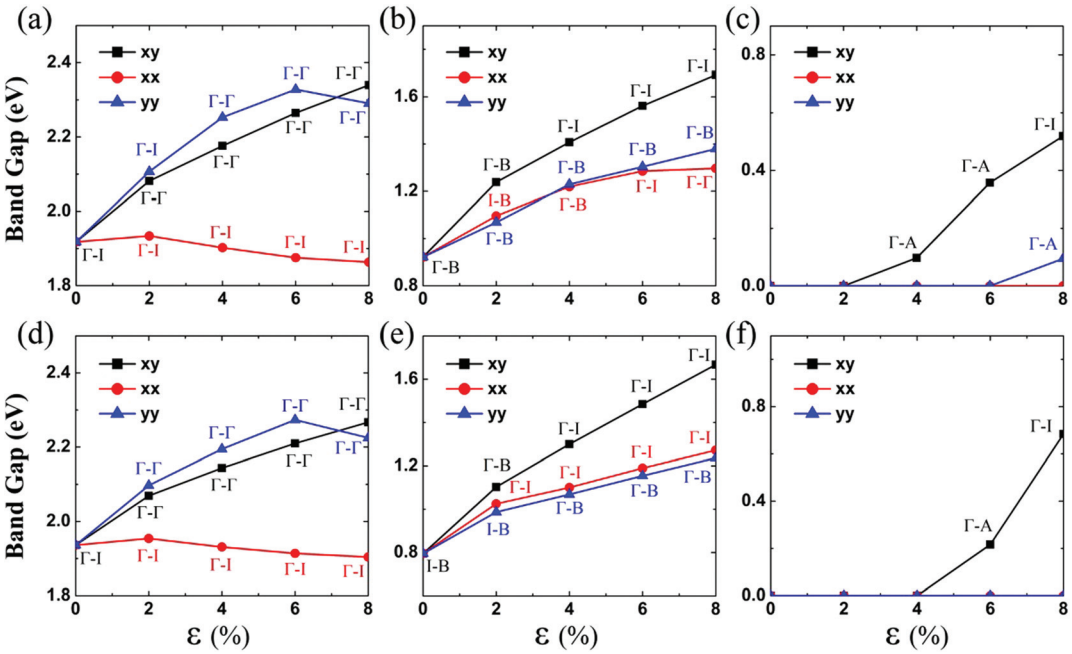

Fig. 2 Computed bandgaps of (a) ZrS_3, (b) $ZrSe_3$, (c) $ZrTe_3$, (d) HfS_3, (e) $HfSe_3$, and (f) $HfTe_3$ monolayers *versus* the biaxial or uniaxial tensile strain, ranging from ε = 0% to 8%. The black lines denote the bandgap *versus* biaxial tensile strain in both the x and y directions. The red lines denote the bandgap *versus* the uniaxial tensile strain in the x direction, and the blue lines denote the bandgap *versus* the uniaxial tensile strain in the y direction. Γ, A and B represent the special points in the first Brillouin zone (Fig. 1(c)), while I refers to either the valence band maximum or conduction band minimum that is not located at the Γ point. Hence, Γ–Γ denotes the direct bandgap, whereas Γ–A, Γ–B and Γ–I denote the indirect bandgap.

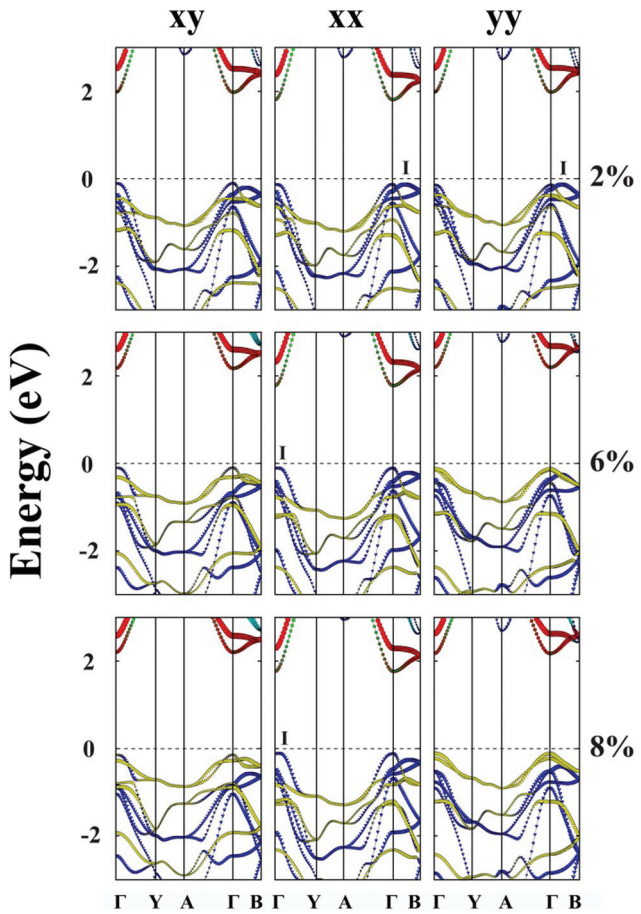

Fig. 4 Computed band structures of strained monolayered ZrS_3 under the biaxial tensile strain in both the *x* and *y* directions (*xy*), or under the uniaxial tensile strain in the *x* direction (*xx*) or the *y* direction (*yy*). The red and green lines illustrate the d_{z^2} orbital and the $d_{x^2-y^2}$ orbital of the Zr atom, respectively. The cyan lines denote the d_{xy}, d_{yz} and d_{xz} orbitals of the Zr atom. The blue lines denote the p_x and p_y orbitals of the S atom, and the yellow lines denote the p_z orbital of the S atom. The dashed lines indicate the Fermi level. The I point refers to the VBM not located at the Γ point.

the ZrS_3 monolayer transforms from an indirect to direct bandgap semiconductor, as both the VBM and CBM are located at the Γ point. This transformation is mainly due to the energy (of the p orbital of the S atom) at the Γ point shifting above the energy at I point, thereby the VBM is changed from I point to Γ point. The CBM however is still located at the Γ point, resulting in a direct bandgap. Moreover, upon increasing the biaxial strain to a high value of ε = 8%, the direct bandgap character is still retained although the bandgap is increased from 1.92 to 2.34 eV.

Likewise, the uniaxial tensile strain of ε = 4% along the *y* direction can also lead to the indirect-to-direct bandgap transition for the ZrS_3 monolayer. The direct bandgap character is maintained even when the strain is as high as 8%. Meanwhile, the uniaxial expansion in the *y* direction initially increases the bandgap from 1.92 to 2.33 eV at ε = 6%, and then slightly reduces the bandgap to 2.29 eV at ε = 8%.

When the monolayered ZrS_3 is subjected to uniaxial tensile strain in the *x* direction, as shown in Fig. 4, the indirect bandgap character is maintained even when the strain is as high as 8%. In addition, uniaxial expansion in the *x* direction only slightly changes the bandgap from 1.92 to 1.93 eV at ε = 2%, while it reduces the bandgap to 1.86 eV at ε = 8%.

Unstained monolayered $ZrSe_3$ is a semiconductor with an indirect bandgap of 0.92 eV (Fig. 3(b)), and the VBM and CBM are located at the Γ and B points, respectively. Both VBM and CBM are mainly contributed by p_x and p_y orbitals of the Se atom. When the monolayered $ZrSe_3$ is subjected to biaxial tensile strain from 2% to 8%, the bandgap increases from 1.24 to 1.69 eV (Fig. 2 and ESI Fig. S3†). The $ZrSe_3$ monolayer remains an indirect bandgap semiconductor, as the VBM is always located at the Γ point, while the CBM shifts from B to I point at ε = 4%. As shown in ESI Fig. S3,† upon increasing the strain to ε = 8%, the CBM is still located at the I point.

Upon applying the uniaxial tensile strain of ε = 2% along the *x* direction to the monolayered $ZrSe_3$, the VBM shifts from the Γ to the I point. Interestingly, at ε = 4%, the VBM shifts back to the Γ point. At ε = 8%, the energy (of the p orbital of the S atom) at the B point shifts above that at the Γ point. Consequently, the CBM shifts from the B point to the Γ point, whereas the VBM is still located at the Γ point, resulting in a direct bandgap. The uniaxial tensile strain in the *x* direction increases the bandgap from 1.10 to 1.30 eV at ε = 8%.

When the monolayered $ZrSe_3$ is subjected to uniaxial tensile strain in the *y* direction, the VBM is always located at the Γ point, and the CBM is always located at the B point. In any event, the uniaxial expansion in the *y* direction can modulate the indirect bandgap from 1.07 to 1.38 eV.

For HfS_3 and $HfSe_3$ monolayers, the strain-dependent bandgap behavior is quite similar to that of ZrS_3 and $ZrSe_3$. The detailed electronic structure *versus* tensile strain for HfS_3 and $HfSe_3$ is shown in ESI Fig. S4–S6.†

Unlike MS_3 and MSe_3, unstrained $ZrTe_3$ and $HfTe_3$ monolayers are predicted to be metals. Importantly, when the $ZrTe_3$ monolayer is subjected to biaxial tensile strain of ε = 4%, it transforms from a metal to semiconductor with an indirect bandgap of 0.10 eV. The VBM and CBM are located at the Γ point and A point, respectively. As shown in Fig. 5, the valence band near the Fermi level is mainly contributed by p_x and p_y orbitals of the Te atom, and the CBM is mainly contributed by the p_z orbital of the Te atom. The energy splitting between the p orbital at Γ point and at A point increases with increasing the biaxial tensile strain, leading to the metal-to-semiconductor transition. At ε = 8% the CBM shifts from A to I point and the bandgap increases to 0.52 eV. Uniaxial expansion in the *y* direction to ε = 8% can open a bandgap of 0.10 eV. In contrast, upon applying uniaxial tensile strain along the *x* direction, the metallic character of the $ZrTe_3$ monolayer is retained even at ε = 8%.

Like $ZrTe_3$, upon applying uniaxial tensile strain along the *x* direction, the metallic character of the $HfTe_3$ monolayer is still retained, even at ε = 8% (ESI Fig. S7†). $HfTe_3$ also keeps the metallic character even under uniaxial stain of ε = 8% in the *y*

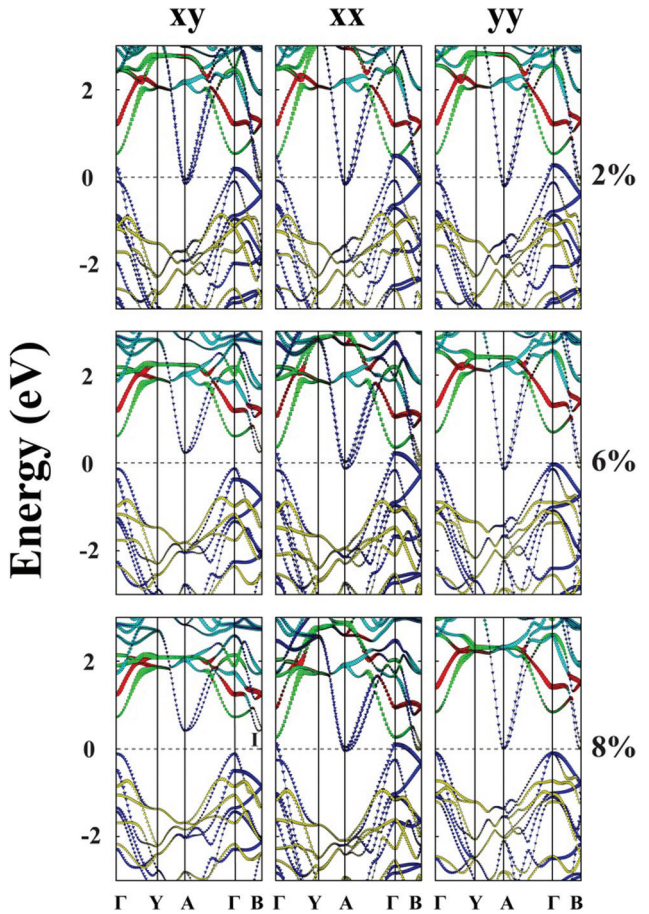

Fig. 5 Computed band structures of strained monolayered $ZrTe_3$ under the biaxial tensile strain (*xy*) in both the *x* and *y* directions, or under the uniaxial tensile strain in the *x* direction (*xx*) or the *y* direction (*yy*). The red lines denote the d_{z^2} orbital of the Zr atom. The green lines denote the $d_{x^2-y^2}$ orbitals of the Zr atom. The cyan lines denote the d_{xy}, d_{yz} and d_{xz} orbitals of the Zr atom. The blue lines denote the p_x and p_y orbitals of the Te atom, and the yellow lines denote the p_z orbital of the Te atom. The dashed lines indicate the Fermi level. The I point refers to the CBM not located at the Γ point.

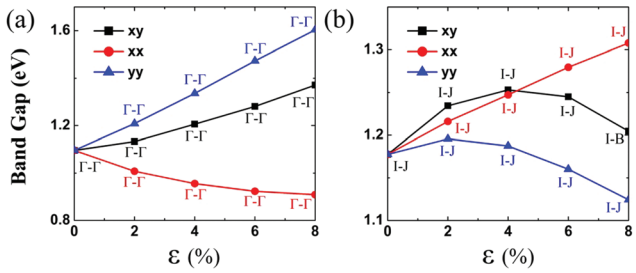

Fig. 6 Bandgap of (a) TiS_3 and (b) NbS_3 monolayers *versus* the biaxial and uniaxial tensile strain ranging from 0% to 8%. The black lines denote the bandgap *versus* biaxial tensile strain both in the *x* and *y* directions. The red lines denote the bandgap *versus* the uniaxial tensile strain in the *x* direction. The blue lines denote the bandgap *versus* the uniaxial tensile strain in the *y* direction.

direction. Only the biaxial tensile strain can open a bandgap of $HfTe_3$, *e.g.*, to 0.22 eV at ε = 6% and to 0.68 eV at ε = 8%. At the two strains, the VBM is located at the Γ point while the CBM is located at the A point and I point, respectively.

TiS_3 and NbS_3

Lastly, the effect of tensile strain on the bandgap of the TiS_3 monolayer is also investigated. The TiS_3 monolayer is a semiconductor with a direct bandgap of 1.08 eV. As illustrated in Fig. 6(a) and 7 and ESI Fig. S8.† Both VBM and CBM are located at the Γ point, consistent with the results of previous studies.[29] The bandgap can increase up to 1.37 eV at the biaxial tensile strain ε = 8%. Likewise, upon applying uniaxial strain along the *y* direction, the direct bandgap character is maintained even at ε = 8%, and the bandgap is enlarged from 1.21 to 1.60 eV. The latter is wider than the enlarged bandgap

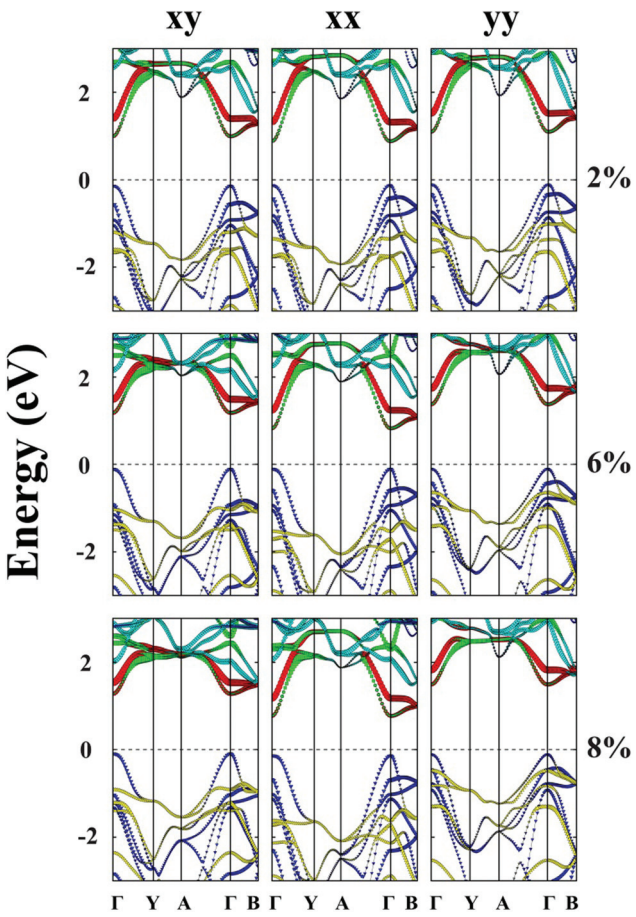

Fig. 7 Computed band structures of the strained monolayered TiS_3 subjected to the biaxial tensile strain both in the *x* and *y* directions (*xy*), the uniaxial tensile strain in the *x* direction (*xx*) or the *y* direction (*yy*). The red and green lines illustrate the d_{z^2} and $d_{x^2-y^2}$ orbitals of the Ti atom, respectively. The cyan lines represent the d_{xy}, d_{yz} and d_{xz} orbitals of the Ti atom. The blue lines represent the p_x and p_y orbitals of the S atom, and the yellow lines show the p_z orbital of the S atom. The dashed lines indicate the Fermi level.

at the biaxial strain of ε = 8%. In contrast, when the monolayered TiS_3 is subjected to uniaxial tensile strain in the x direction, although its direct gap character is maintained even at ε = 8%, the bandgap is actually reduced from 1.08 eV to 1.01 eV at ε = 2%, and to 0.91 eV at ε = 8%. The opposite trend of bandgap change is due to the downward shift of CBM at the Γ point. Here, the VBM is mainly contributed by p_x and p_y orbitals of the S atom, while the CBM is mainly contributed by d_{z^2} and $d_{x^2-y^2}$ orbitals of the Ti atom.

Bulk NbS_3 is a triclinic structure with the space group of $P1$. As shown in Fig. 6(b) and ESI Fig. S8,† the unstrained NbS_3 monolayer is a semiconductor with an indirect bandgap of 1.18 eV. The CBM, located on the Γ–B line, is mainly contributed by the d_{xz} orbital of the Nb atom, while the VBM, located on the Y–A line, is mainly contributed by the d_{z^2} and $d_{x^2-y^2}$ orbitals of the Nb atom. The NbS_3 monolayer retains its indirect bandgap, regardless of the biaxial and uniaxial tensile strain. Moreover, the strain can only change the bandgap modestly.

Conclusions

In conclusion, we present a comprehensive study of the effect of tensile strain on the electronic structures of transition-metal trichalcogenide monolayers, based on density functional theory computations. Our computations predict that MS_3 and MSe_3 (M = Ti, Zr, Hf, Nb) monolayers are all semiconductors, while MTe_3 monolayers are metals. Both ZrS_3 and HfS_3 monolayers can undergo an indirect-to-direct bandgap transition with increasing tensile strain. The indirect bandgap of $ZrSe_3$ and $HfSe_3$ monolayers increases with the tensile strain, but the indirect character is retained in most cases. The $ZrTe_3$ and $HfTe_3$ monolayers can be transformed from a metal to semiconductor with an indirect bandgap at ε = 4% and ε = 6%, respectively. The TiS_3 monolayer can retain its direct bandgap under either the biaxial or uniaxial strain, ranging from ε = 0% to 8%. The NbS_3 monolayer retains its indirect bandgap, regardless of the tensile strain. Overall, the bandgaps of MX_3 monolayers can be modulated from 0.68 eV to 2.34 eV at $\varepsilon \leq 8\%$.

We note that as the atomic number of X increases from S to Te, the bandgap decreases significantly. For instance, the bandgap of ZrS_3 is about 1.92 eV, whereas the bandgap of $ZrSe_3$ is 0.92 eV. Note also that in their TMDC counterparts, the ZrS_2 monolayer can transform from an indirect to a direct bandgap semiconductor when the uniaxial tensile strain is at ε = 8%.[51] The TiS_2 monolayer can also undergo the indirect-to-direct bandgap transition under the uniaxial strain of ε = 10%. In contrast, the ZrS_3 and HfS_3 monolayers can undergo the indirect-to-direct bandgap transition at a much lower tensile strain (ε = 2%). It seems that the indirect-to-direct bandgap transition can be induced more easily for the MX_3 monolayers than for their MX_2 counterparts by the tensile strain. The direct bandgap character and high bandgap tunability by strain as well as the availability of metallic and semiconducting properties of MTe_3 (M = Hf and Zr) provide new opportunities for designing artificial layered structures for applications in optoelectronics and flexible electronics.

Acknowledgements

This work was supported in US by the National Science Foundation (NSF) through the Nebraska Materials Research Science and Engineering Center (MRSEC) (grant No. DMR-1420645) NSF, the UNL Nebraska Center for Energy Sciences Research, and the UNL Holland Computing Center. This study was supported in China by the NSFC (51472073), the program of the China Scholarship Council (No. 201408130035), the Foundation of Hebei Education Department (QN20131088), and the Peiyu Foundation of North China University of Science and Technology (GP201309).

References

1 A. Splendiani, L. Sun, Y. Zhang, T. Li, J. Kim, C. Chim, G. Galli and F. Wang, *Nano Lett.*, 2010, **10**, 1271–1275.
2 B. Radisavljevic, A. Radenovic, J. Brivio, V. Giacometti and A. Kis, *Nat. Nanotechnol.*, 2011, **6**, 147–150.
3 Y. Yoon, K. Ganapathi and S. Salahuddin, *Nano Lett.*, 2011, **11**, 3768–3773.
4 B. Radisavljevic, M. B. Whitwick and A. Kis, *ACS Nano*, 2011, **5**, 9934–9938.
5 Y. Ma, Y. Dai, M. Guo, C. Niu, Y. Zhu and B. Huang, *ACS Nano*, 2012, **6**, 1695–1701.
6 H. Wang, L. Yu, Y. Lee, Y. Shi, A. Hsu, M. L. Chin, L. Li, M. Dubey, J. Kong and T. Palacios, *Nano Lett.*, 2012, **12**, 4674–4680.
7 K. Kang, S. Xie, L. Huang, Y. Han, P. Y. Huang, K. F. Mak, C. Kim, D. Muller and J. Park, *Nature*, 2015, **520**, 656–660.
8 Y. Li, Z. Zhou, S. Zhang and Z. Chen, *J. Am. Chem. Soc.*, 2008, **130**, 16739–16744.
9 Q. H. Wang, K. Kalantar-Zadeh, A. Kis, J. N. Coleman and M. S. Strano, *Nat. Nanotechnol.*, 2012, **7**, 699–712.
10 M. Chhowalla, H. S. Shin, G. Eda, L. Li, K. P. Loh and H. Zhang, *Nat. Chem.*, 2013, **5**, 263–275.
11 K. F. Mak, C. Lee, J. Hone, J. Shan and T. F. Heinz, *Phys. Rev. Lett.*, 2010, **105**, 136805.
12 V. Nicolosi, M. Chhowalla, M. G. Kanatzidis, M. S. Strano and J. N. Coleman, *Science*, 2013, **340**, 1226419.
13 J. N. Coleman, M. Lotya, A. O. Neill, S. D. Bergin, P. J. King, U. Khan, K. Young, A. Gaucher, S. De, R. J. Smith, *et al.*, *Science*, 2011, **331**, 568–571.
14 R. J. Smith, P. J. King, M. Lotya, C. Wirtz, U. Khan, S. De, A. O'Neill, G. S. Duesberg, J. C. Grunlan and G. Moriarty, *Adv. Mater.*, 2011, **23**, 3944–3948.
15 L. Brattas and A. Kjekshus, *Acta Chem. Scand.*, 1972, **26**, 3441–3449.
16 S. Furuseth, L. Brattås and A. Kjekshus, *Acta Chem. Scand.*, 1975, **29**, 623–631.
17 S. Kikkawa, N. Ogawa, M. Koizumi and Y. Onuki, *J. Solid State Chem.*, 1982, **41**, 315–322.

18 J. Rijnsdorp and F. Jellinek, *J. Solid State Chem.*, 1978, **25**, 325–328.
19 S. Kikkawa, M. Koizumi, S. Yamanaka, Y. Onuki and S. Tanuma, *Phys. Status Solidi A*, 1980, **61**, K55–K57.
20 M. Hoesch, X. Cui, K. Shimada, C. Battaglia, S. Fujimori and H. Berger, *Phys. Rev. B: Condens. Matter*, 2009, **80**, 75423.
21 D. Pacilé, M. Papagno, M. Lavagnini, H. Berger, L. Degiorgi and M. Grioni, *Phys. Rev. B: Condens. Matter*, 2007, **76**, 155406.
22 P. Starowicz, C. Battaglia, F. Clerc, L. Despont, A. Prodan, H. van Midden, U. Szerer, A. Szytuła, M. G. Garnier and P. Aebi, *J. Alloys Compd.*, 2007, **442**, 268–271.
23 D. W. Bullett, *J. Phys. C: Solid State Phys.*, 1979, **12**, 277–281.
24 H. W. Myron, B. N. Harmon and F. S. Khumalo, *J. Phys. Chem. Solids*, 1981, **42**, 263–267.
25 K. Stöwe and F. R. Wagner, *J. Solid State Chem.*, 1998, **138**, 160–168.
26 C. Felser, E. W. Finckh, H. Kleinke, F. Rocker and W. Tremel, *J. Mater. Chem.*, 1998, **8**, 1787–1798.
27 J. O. Island, M. Barawi, R. Biele, A. Almazán, J. M. Clamagirand, J. R. Ares, C. Sánchez, H. S. van der Zant, J. V. Álvarez and R. D'Agosta, *Adv. Mater.*, 2015, **27**, 2595–2601.
28 A. Lipatov, P. Wilson, M. Shekhirev, J. Teeter, R. Netusil and A. Sinitskii, *Nanoscale*, 2015, **7**, 12291–12296.
29 J. Dai and X. C. Zeng, *Angew. Chem., Int. Ed.*, 2015, **54**, 7572–7576.
30 Y. Jin, X. Li and J. L. Yang, *Phys. Chem. Chem. Phys.*, 2015, **17**, 18665–18669.
31 J. O. Island, M. Buscema, M. Barawi, J. M. Clamagirand, J. R. Ares, C. Sánchez, I. J. Ferrer, G. A. Steele, H. S. van der Zant and A. Castellanos Gomez, *Adv. Opt. Mater.*, 2014, **2**, 641–645.
32 H. G. Grimmeiss, A. Rabenau, H. Hahn and P. Ness, *Z. Elektrochem.*, 1961, **65**, 776.
33 D. W. Bullett, *J. Solid State Chem.*, 1980, **33**, 13–16.
34 G. Perluzzo, A. A. Lakhani and S. Jandl, *Solid State Commun.*, 1980, **35**, 301–304.
35 K. Patel, J. Prajapati, R. Vaidya and S. G. Patel, *Bull. Mater. Sci.*, 2005, **28**, 405–410.
36 K. Patel, J. Prajapati, R. Vaidya and S. G. Patel, *Indian J. Phys.*, 2005, **79**, 373.
37 A. Zwick, M. A. Renucci and A. Kjekshus, *J. Phys. C: Solid State Phys.*, 1980, **13**, 5603.
38 J. A. Wilson, *Phys. Rev. B: Condens. Matter*, 1979, **19**, 6456.
39 P. Johari and V. B. Shenoy, *ACS Nano*, 2012, **6**, 5449–5456.
40 L. Kou, T. Frauenheim and C. Chen, *J. Phys. Chem. Lett.*, 2013, **4**, 1730–1736.
41 A. Castellanos-Gomez, R. Roldán, E. Cappelluti, M. Buscema, F. Guinea, H. S. van der Zant and G. A. Steele, *Nano Lett.*, 2013, **13**, 5361–5366.
42 H. J. Conley, B. Wang, J. I. Ziegler, R. F. Haglund Jr., S. T. Pantelides and K. I. Bolotin, *Nano Lett.*, 2013, **13**, 3626–3630.
43 Y. Y. Hui, X. Liu, W. Jie, N. Y. Chan, J. Hao, Y. Hsu, L. Li, W. Guo and S. P. Lau, *ACS Nano*, 2013, **7**, 7126–7131.
44 K. He, C. Poole, K. F. Mak and J. Shan, *Nano Lett.*, 2013, **13**, 2931–2936.
45 C. R. Zhu, G. Wang, B. L. Liu, X. Marie, X. F. Qiao, X. Zhang, X. X. Wu, H. Fan, P. H. Tan, T. Amand and B. Urbaszek, *Phys. Rev. B: Condens. Matter*, 2013, **88**, 121301.
46 Q. Yue, J. Kang, Z. Shao, X. Zhang, S. Chang, G. Wang, S. Qin and J. Li, *Phys. Lett. A*, 2012, **376**, 1166–1170.
47 A. Ramasubramaniam, D. Naveh and E. Towe, *Phys. Rev. B: Condens. Matter*, 2011, **84**, 205325.
48 Y. Zhou, Z. Wang, P. Yang, X. Zu, L. Yang, X. Sun and F. Gao, *ACS Nano*, 2012, **6**, 9727–9736.
49 W. S. Yun, S. W. Han, S. C. Hong, I. G. Kim and J. D. Lee, *Phys. Rev. B: Condens. Matter*, 2012, **85**, 033305.
50 S. Bhattacharyya and A. K. Singh, *Phys. Rev. B: Condens. Matter*, 2012, **86**, 075454.
51 (*a*) P. Lu, X. J. Wu, W. L. Guo and X. C. Zeng, *Phys. Chem. Chem. Phys.*, 2012, **14**, 13035–13040; (*b*) H. Guo, N. Lu, L. Wang, X. Wu and X. C. Zeng, *J. Phys. Chem. C*, 2014, **118**, 7242–7249.
52 N. Lu, H. Guo, L. Li, J. Dai, L. Wang, W. Mei, X. Wu and X. C. Zeng, *Nanoscale*, 2014, **6**, 2879–2886.
53 L. Kou, A. Du, C. Chen and T. Frauenheim, *Nanoscale*, 2014, **6**, 5156.
54 G. Kresse and J. Furthmüller, *Phys. Rev. B: Condens. Matter*, 1996, **54**, 11169.
55 G. Kresse and D. Joubert, *Phys. Rev. B: Condens. Matter*, 1999, **59**, 1758.
56 A. D. Becke, *J. Chem. Phys.*, 1986, **84**, 4524.
57 J. J. Klimeš, D. R. Bowler and A. Michaelides, *J. Phys.: Condens. Matter*, 2010, **22**, 22201.
58 J. Heyd, G. E. Scuseria and M. Ernzerhof, *J. Chem. Phys.*, 2006, **124**, 219906.